Journal of
Medical Imaging

MedicalImaging.SPIEDigitalLibrary.org

Determination and verification of the x-ray spectrum of a CT scanner

Ahmad Ibrahim Hassan
Martin Skalej
Helmut Schlattl
Christoph Hoeschen

Ahmad Ibrahim Hassan, Martin Skalej, Helmut Schlattl, Christoph Hoeschen, "Determination and verification of the x-ray spectrum of a CT scanner," *J. Med. Imag.* **5**(1), 013506 (2018), doi: 10.1117/1.JMI.5.1.013506.

Journal of Medical Imaging 5(1), 013506 (Jan–Mar 2018)

Determination and verification of the x-ray spectrum of a CT scanner

Ahmad Ibrahim Hassan,[a,b,*] Martin Skalej,[a] Helmut Schlattl,[c] and Christoph Hoeschen[b]
[a]Otto von Guericke Universität Magdeburg, Universitätsklinikum Magdeburg A.ö.R., Institut für Neuroradiologie, Magdeburg, Deutschland, Germany
[b]Otto von Guericke Universität, Institut für Medizintechnik, Fakultät für Elektrotechnik und Informationstechnik Universitätsplatz, Magdeburg, Deutschland, Germany
[c]Institute of Radiation Protection, Helmholtz Zentrum München—German Research Center for Environmental Health, Neuherberg, Deutschland, Germany

Abstract. The accuracy of Monte Carlo (MC) simulations in estimating the computed tomography radiation dose is highly dependent on the proprietary x-ray source information. To address this, this study develops a method to precisely estimate the x-ray spectrum and bowtie (BT) filter thickness of the x-ray source based on physical measurements and calculations. The static x-ray source of the CT localizer radiograph was assessed to measure the total filtration at the isocenter for the x-ray spectrum characterization and the BT profile (air-kerma values as a function of fan angle). With these values, the utilized BT filter in the localizer radiograph was assessed by integrating the measured air kerma in a full 360-deg cycle. The consistency observed between the integrated BT filter profiles and the directly measured profiles pointed to the similarity in the utilized BT filter in terms of thickness and material between the static and rotating x-ray geometries. Subsequently, the measured air kerma was used to calculate the BT filter thickness and was verified using MC simulations by comparing the calculated and measured air-kerma values, where a very good agreement was observed. This would allow a more accurate computed tomography simulation and facilitate the estimation of the dose delivered to the patients. [DOI: 10.1117/1.JMI.5.1.013506]

Keywords: CT localizer radiograph; multidetector CT; radiation dose; Monte Carlo simulations; x-ray spectrum; bowtie filter.

Paper 17076SSRRR received Mar. 24, 2017; accepted for publication Jan. 10, 2018; published online Feb. 7, 2018.

1 Introduction

The use of multidetector computed tomography (MDCT) has significantly increased the overall population's exposure to radiation from computed tomography (CT) sources.[1–5] This increase is primarily due to patients' relatively high radiation exposure during each examination, as well as the large number of examinations. To better understand the risks associated with MDCT examinations, scientists have attempted to calculate the radiation dose delivered to individual patients, both that delivered to each organ as well as the average collective dose.[6–21] These values are typically estimated using Monte Carlo (MC) software packages.[22] These packages require information about scanner geometry, in particular the focal spot to isocenter distance, fan angle, and z-axis collimation, which are all available in scanner documentation.[23] It is crucial to obtain information about the energy spectra to accurately estimate the dose from an MDCT scan using MC simulation methods.[24] Understanding the energy spectra requires prior knowledge of the utilized filtration, such as bowtie (BT) filter thickness. Information about the design and composition of the BT filter is proprietary and differs for different scanner manufacturers. It is convenient to measure the BT attenuation in service mode, where the x-ray source is in a static position and the appropriate BT filter is specified by the manufactures nomenclature. It is often assumed that the resulting BT thickness profiles of the static sources agree with those of the rotating sources without experimental verification.

Different approaches have been used to estimate various characteristics of static and rotating x-ray sources, specifically the x-ray spectra and BT filter thickness.[25–33] For static x-ray sources, Turner et al. describe a method for estimating x-ray spectra based on physical measurements of the half-value layer (HVL).[25] In the same study, the static x-ray source was used to estimate the BT filter profile by measuring air kerma as a function of the fan angle, thereby determining an equivalent filter. This method can be used to estimate the number of photons in the off-centerline spectra; however, using this method, it is not possible to match the relative number of photons with the spectral shape because only one material thickness (aluminum) is varied.

For rotating sources, Boone proposed a measurement method utilizing a dosimeter placed at the edge of an x-ray field generated by a rotating source.[26] They then used the air-kerma rate to determine the angle-dependent BT filter attenuation. Theoretically, this method effectively characterizes the BT filter used in commercial CT scanners. There are some limitations, however, including the need for real-time dosimeter readings with sufficient sensitivity and high temporal resolution. Another challenge is the inability to determine the HVL of a rotating x-ray source when characterizing the x-ray spectrum. These limitations were overcome in subsequent studies.[27–29] In addition, a method was later proposed that allowed for an angle-dependent estimation of the x-ray spectrum for rotating sources.[34] This technique was experimentally tested using a

---

*Address all correspondence to: Ahmad Ibrahim Hassan, E-mail: ahmad.hassan@ovgu.de

2329-4302/2018/$25.00 © 2018 SPIE

CT scanner, and the results were compared with data provided by the manufacturer. The results demonstrate that the measurement of the incident spectrum over a wide range of angular trajectories is possible with both a high level of accuracy and stability. In addition, Yang et al. proposed a new method to measure CT filter profiles using a linear array solid-state detector for rotating x-ray sources.[35] This approach utilizes both accurate geometric calibration and high angular resolution.

For all of the aforementioned approaches, determination of the BT filter thickness was made using either physical measurements of a static source, using a scanner that was successfully put into service mode (trusting the manufacturers' nomenclature of the BT-filter) or measurements of a rotating x-ray source utilized in the clinical protocols.[25–33] Some studies assessed the physical measurements by comparing the measured air kerma with the simulated air kerma using MC simulation methods,[25,31–33] while other studies did not assess their physical measurements at all,[27–30] which calls into question the accuracy of the calculated BT filter thicknesses. This study investigates the possibility of accurately deriving the BT filter thickness profile to be used in clinical protocols using only physical measurements of a static and rotating x-ray source, without the need for time-resolving measurements. This method will enable researchers to obtain an accurate BT filter thickness for the actual protocol used. To effectively characterize the BT attenuation profile, the air kerma across the fan angle of the x-ray source is measured utilizing the static x-ray source of a CT localizer radiograph (optionally the service mode could be used). The same measurements are performed for the rotating x-ray source used in clinical protocols. The resulting profiles of the BT filter are then qualitatively compared with the BT profiles from the static x-ray source. This study introduces a new theoretical method for making such a comparison possible. This method involves mathematically integrating the measured profile of the static x-ray source across all incident angles in a full 360-deg cycle. The integrated BT filter profile is then compared with the measured BT profile of the rotating x-ray source used in clinical protocols. These results could provide a more accurate representation of the BT filter utilized in the actual acquisition scan and more substantially demonstrate whether this method is sufficient to achieve accurate BT filter thickness estimates for different operational modes of the x-ray source (stationary and rotating).

In this paper, physical measurements made using the CT scanner are presented along with the methodologies necessary to calculate the BT filter thickness. The accuracy of the resulting BT filter thickness is then assessed by comparing the results of MC simulations with physical measurements of static x-ray sources of the CT localizer radiograph. Similarly, the results of experimental measurements for rotating sources used in the clinical protocols are compared with the simulated MC simulations of multiple CT dose index (CTDI) phantoms.

2 Materials and Methods

2.1 *CT Scanner Model*

All measurements were performed using a SOMATOM Definition 64 CT scanner (Siemens Medical Solutions, Forchheim, Germany).[36] The x-ray tube anode angle was 7 deg. The distances from the focal spot to the isocenter (SID) and the detector (SDD) were 595 and 1085 mm, respectively. The scanner operated in both axial and helical modes at tube voltages of 80, 100, 120, and 140 kV. Two different focal spots were used, with dimensions of $0.7 \times 0.7\ \mathrm{mm}^2$ and $0.9 \times 1.1\ \mathrm{mm}^2$ corresponding to small and large focal spots, respectively. The system operated at different x-ray beam collimations, given in $N \times T$ format, where N represents the number of data channels and T represents the nominal width of each data channel. For this study, x-ray collimations of 3.6 and 38.4 mm were used for static and rotating x-ray sources, respectively. The system is equipped with a BT filter, which is used to compensate for the beam-hardening effect resulting from the variation in the body thickness across the transverse sections of the body. The BT filters are also used to reduce unnecessary patient dose at the periphery of the body.

2.2 *Ionization Chamber*

An ionization chamber type 30009 connected to a Unidos electrometer (PTW, Freiburg, Germany) was used to measure the physical air kerma. The nominal active volume of the ionization chamber was $3.14\ \mathrm{cm}^3$, with a sensitive measuring length of 10 cm and an outer diameter of 0.9 cm. The homogeneity of the detector response was less than ±5% for (70 to 150) kV.[37]

2.3 *Nomex Multimeter*

The Nomex multimeter is a noninvasive device consisting of electronics and multiple channels of silicon semiconductor detectors according to IEC 61674.[38] The system was approved as a diagnostic dosimeter by the German National Metrology Institute, PTB.[39] The Nomex device was calibrated for many different imaging modalities, including radiography, fluoroscopy, mammography (Mo/Mo, Mo/Rh, W/Al, W/Rh, W/Ag, and Rh/Rh), and CT.[40] The Nomex multimeter was designed for the purpose of measuring different quantities during one single radiation exposure, including air kerma, air-kerma rate, tube voltage, and total filtration (TF).

In this study, we use the Nomex multimeter to measure the TF for the following tube voltages: 80, 100, 120, and 140 kV. The essential parts of the Nomex multimeter system are shown in Fig. 1. Parts #1 and #2 represent the multichannel detector and the electronic areas, respectively. Part #3 represents the location of the central axis of the source. Part #4 (the shaded gray area) is illustrated by the 1-mm width bar that identifies the center of the 3-mm wide measurement area. This measurement area indicates the active detector zone for the measurements of TF of the CT scan. The measurement area shown in gray must be fully irradiated. The measurements of the estimated TF area have an accuracy of ±10%, or 0.5 mm.[41] Part #5 indicates the status of the device: for example, a green led light indicates that the device is ready for use.

2.4 *Physical Measurements*

2.4.1 *Static x-ray source measurements*

Most MDCT scanners have more than one BT filter. These BT filters are dependent on the tube voltage, and, more importantly, on the selected field of view (FOV). A large field of view (LFOV) requires a correspondingly wide filter to cover the entire fan beam when scanning the patient. Likewise, clinical protocols for small FOVs (SFOVs) call for a small BT filter due to the reduced diameter of the scanned area. For this study, CT localizer radiographs of child neck protocols and adult

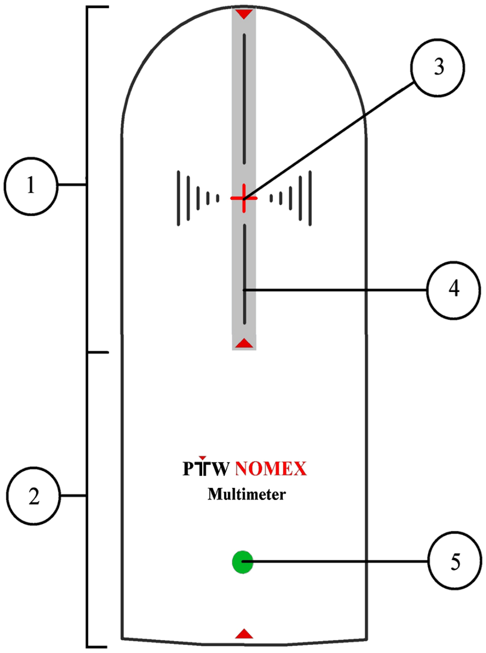

Fig. 1 The Nomex multimeter active area in the measurement of the TF for CT scan.

abdomen protocols were selected to represent SFOVs and LFOVs, respectively. The static x-ray source was positioned at 90 deg, and the patient table was adjusted such that it was outside the measuring field. Air kerma was measured across the fan angles using a plastic ruler. The ruler dimensions were 780, 60, and 8 mm in the x, y, and z-axes, respectively.

A lathe was then used to drill 29, 1-cm-diameter holes in a row, spaced 2 cm from isocenter to isocenter. The tolerance for all dimensions in the manufactured ruler was ±0.1 mm. The ruler was placed across the opening of the CT gantry, and the ionization chamber was placed in the opening holes within the center of the collimation along the z-axis of the scanner, as shown in Fig. 2. Measurements were taken for tube voltages of 80, 100, 120, and 140 kV, while keeping the default settings for the other parameters constant. The parameters used for the experiments were the following: tube current of 300 mA, collimation width of 3.6 mm, and exposure times of 2.7 and 5.3 s for SFOV and LFOV CT localizer radiographs, respectively.

2.4.2 *Half-value layer measurements*

The HVL was measured for tube voltages of 80, 100, 120, and 140 kV. The static x-ray source of the CT localizer was placed at a 90 deg position because the x-ray source cannot be placed at the standard position (180 deg) when collecting HVL measurements, as shown in Fig. 3. The ionization chamber was placed at the isocenter hole of the plastic ruler in the direction of the central ray. The default settings used in the static x-ray source experiments (Sec. 2.4.1) were also used in the HVL experiments for both SFOV and LFOV CT localizer radiographs. The HVL was estimated by increasing the thickness of the aluminum layers until the air kerma was equal to one half of the measured air kerma free-in-air without aluminum layers.

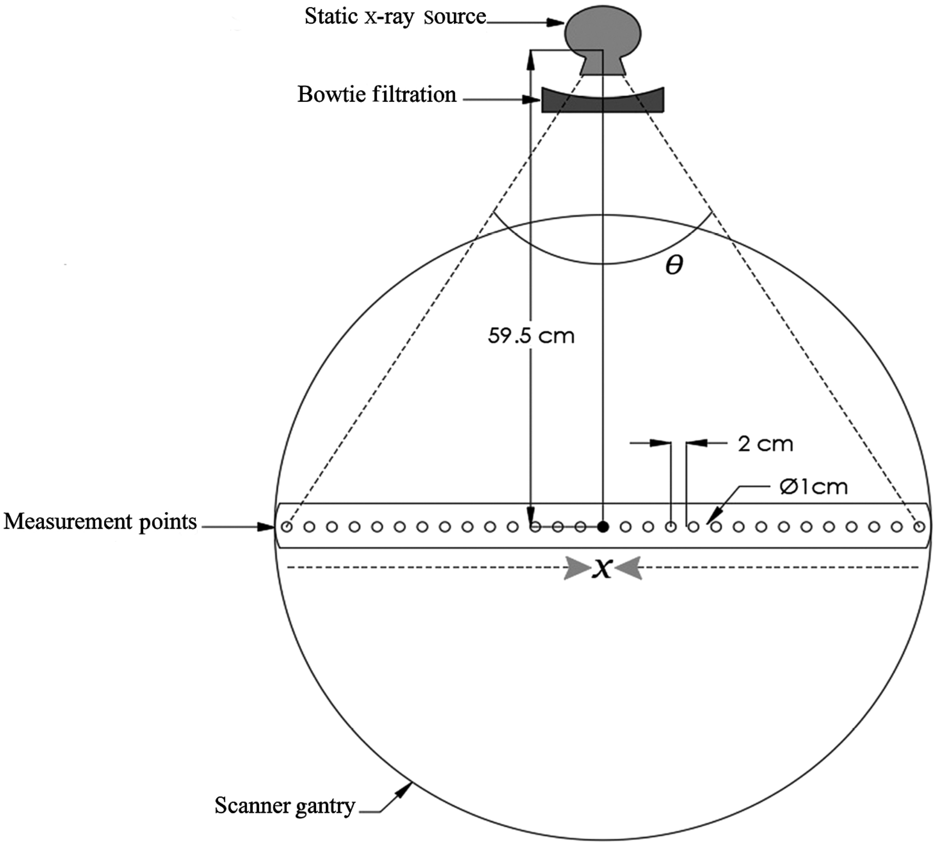

Fig. 2 Schematic view of BT profile measurements across the fan angle of the static x-ray source.

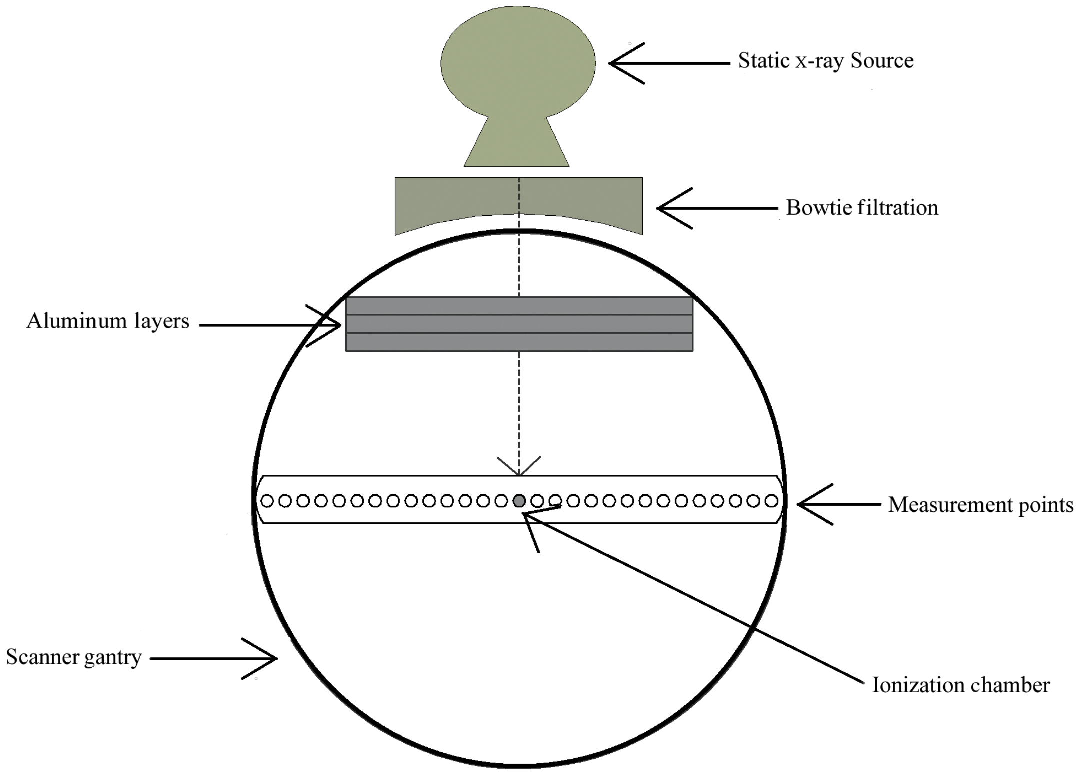

Fig. 3 Experimental set up of HVL measurements.

2.4.3 *Rotating x-ray source measurements*

The attenuation of the BT profile was measured as a function of fan angle for the rotating x-ray source. These physical measurements were obtained for comparison purposes only. The ruler was positioned across the CT gantry, and the ionization chamber was placed in the opening holes within the center of the collimation along the z-axis of the scanner, as shown in Fig. 4. Two different clinical protocols were selected to represent SFOV and LFOV, and the rotating source in both protocols was operated in the helical mode. For SFOV, the child neck and abdomen protocols were selected using default settings of 90-mA tube current and 38.4-mm collimation width. The scan times were 7 s for the child neck protocol and 1 s for the child abdomen protocol. For LFOV, the clinical protocols of the adult abdomen and thorax were used with settings of 4 s scan time, 38.4 mm collimation width, and tube currents of 210 and 110 mA for abdomen and thorax protocols, respectively. Notably, all measurements were obtained at a tube voltage of 120 kV, which is commonly used in clinical protocols.

2.5 *Integration of the Static X-Ray Source Measurements*

Several BT filters are used in MDCT studies today. The selection of a particular BT filter depends on the tube voltage, and, more importantly, the FOV. The same BT filter can be used in different operational modes of the x-ray source. To evaluate this, a direct comparison can be made between the BT filter profiles experimentally measured as a function of angle for both static and rotating x-ray sources. However, the different status of the static and rotating x-ray sources made such a direct comparison invalid. In this study, a new method (hereafter referred to as the integration method) is proposed to make the measurements of static and rotating sources comparable. The method utilizes an integrated x-ray source, resulting from the integration of static x-ray source measurements across a 360-deg cycle. The resulting estimate of the BT profiles from the integration of static x-ray source measurement values was then compared with the directly measured BT profiles of the actual rotating x-ray source of the clinical protocols. This provided useful information about the consistency or discrepancy of the BT filters used for static and rotating x-ray sources. This could eliminate the necessity of relying on time-resolving measurements to calculate the BT filter thickness of a given scanner.

Figure 5 illustrates the relationship between the integrated static x-ray source and the static x-ray source used in this experiment. For the integrated static source, the origin of the coordinate system is placed at the isocenter (x_0). We define (S_α) as the point at which the source makes an angle (α) with the positive x-axis. Using this terminology, the static case can be viewed as a unique configuration of the integrated static case (when $\alpha = \frac{\pi}{2}$); hence, the position of the static source can be described by the coordinates (0, R). This case is denoted by (S), where $S = S_{\frac{\pi}{2}}$.

The experimental measurements of the static x-ray source can help determine whether the attenuation profile of the BT filter can be inferred from the integration of the static x-ray source values. The measurement procedures are explained in Sec. 2.4.1, and Fig. 2 shows a detailed schematic of the experimental geometry and setup. The static x-ray source was positioned at $\frac{\pi}{2}$, and the ionization chamber was placed in the opening holes of the ruler laid across the x-axis such that the active length of the ionization chamber was centered along the z-axis of the scanner.

The ionization chamber was shifted across the measurement points to the isocenter ($x_0 \coloneqq 0$) by a distance of

$$x_j = j\Delta x, \tag{1}$$

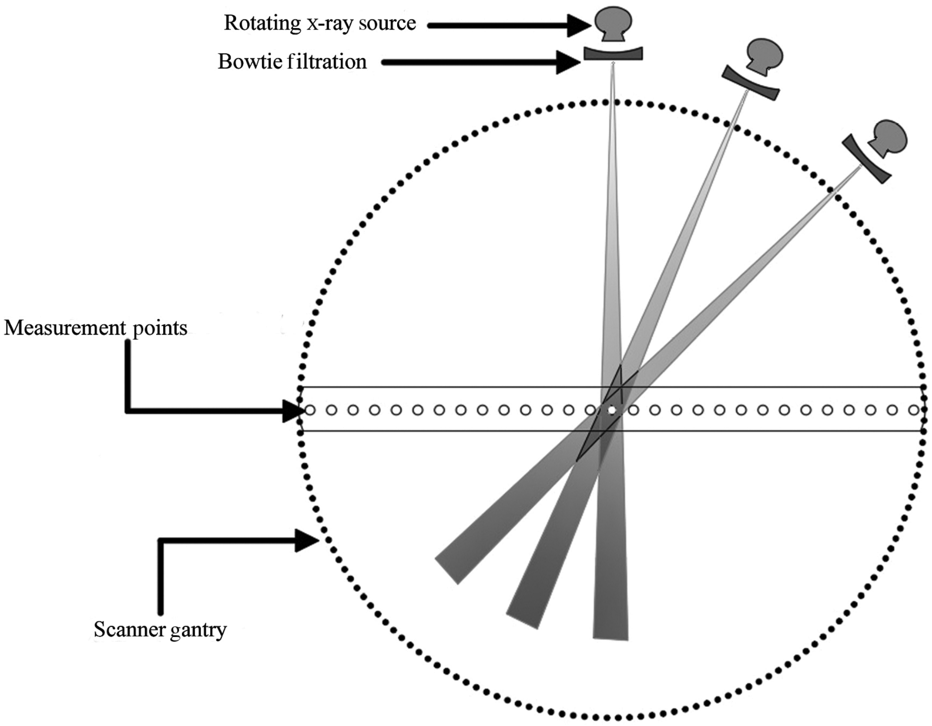

Fig. 4 Experimental scheme of BT profile measurements of attenuation of the rotating x-ray source of the clinical protocols.

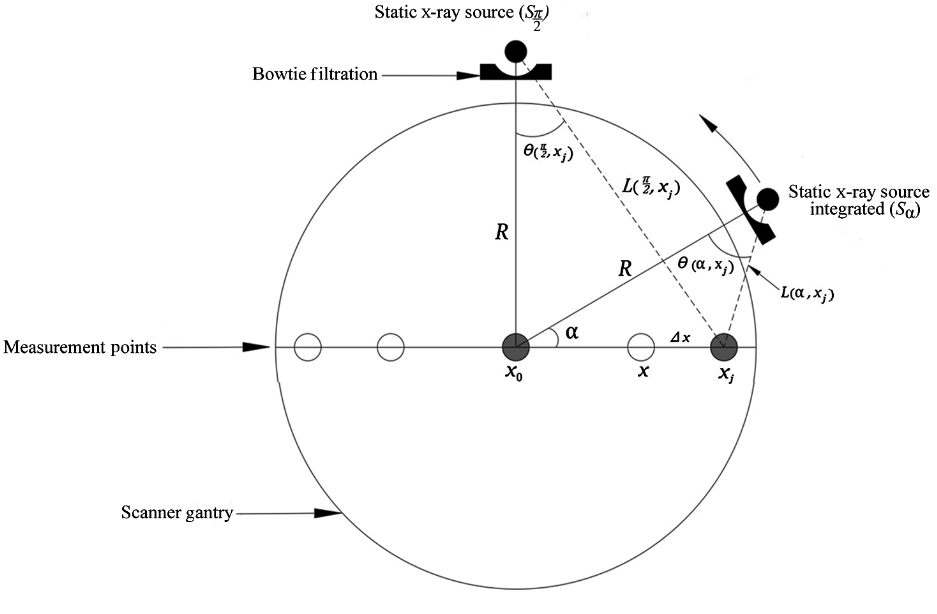

Fig. 5 Schematic view of the geometrical relationship between a static x-ray source and the integrated static x-ray source resulting from the integration method.

where $j = -14, \ldots 0, \ldots 14$ (the number of measurement points placed across x-axis $= 29$) and $\Delta x = 2$ cm.

For static sources, the distance from the x-ray source to the measurement points $L(\frac{\pi}{2}, x_j)$ is given as

$$L\left(\frac{\pi}{2}, x_j\right) = \sqrt{R^2 + x_j^2} = \sqrt{R^2 + (j\Delta x)^2}. \tag{2}$$

For the integrated static sources, S_α, the distance between the x-ray source and a measurement point x_j, is defined by $L(\alpha, x_j)$

$$L(\alpha, x_j) = \sqrt{x_j^2 + R^2 - 2Rx_j \cos \alpha}. \tag{3}$$

The angle $\theta(\alpha, x_j)$ is defined as the fan angle between the x-ray source and the measurement points relative to the central ray. For static sources, this angle can be calculated using

$$\theta\left(\frac{\pi}{2}, x_j\right) = \arctan\left(\frac{j\Delta x}{R}\right). \tag{4}$$

For the integrated static sources, the angle can be calculated as

$$\theta(\alpha, x_j) = \arcsin\left[\frac{x_j \sin\alpha}{(\alpha, x_j)}\right]. \tag{5}$$

The air kerma-length-product for any of the measurement points across the x-axis is a function of the distance from, and the angles to, the source. The air kerma-length-product at the point x_j is denoted by $KL(\alpha, x_j)$ for the integrated static source S_α, and thus $KL(\frac{\pi}{2}, x_j)$ denotes the air kerma at the point x_j for the static source S. At the isocenter point x_0, KL is the same for both the static and integrated static cases for any angle α. This can be written as

$$KL\left(\frac{\pi}{2}, x_0\right) = KL(\alpha, x_0) = KL_{\text{isocenter}}. \tag{6}$$

At each of the measurement points, the relative air-kerma length product for the BT filter across the fan beam is computed as

$$KL\left(\frac{\pi}{2}, x_0\right) = KL(\alpha, x_0) = KL(\alpha, x_j)\frac{L(\alpha, x_j)}{R}. \tag{7}$$

This formula is valid as long as the field length remains smaller than the length of the employed pencil ionization chamber (10 cm). In this case, the measurement field length S is proportional to the distance L. Thus,

$$K \sim \frac{1}{L^2} \quad \text{and} \quad S \sim L,$$

so that

$$KL \sim \frac{1}{L},$$

where K = air kerma.

The total air-kerma length product at the point x_j of the integrated static x-ray source is denoted by $KL(x_j)$. This KL profile at each measurement point is calculated from the static source profile. This is done by integrating the x-ray at all beam angles of the integrated static source, taking into account the distance between the source and the measurement points. In this case, the total air-kerma length product of the integrated static source having completed a full 360-deg cycle is calculated as

$$KL(x_j) = \int_0^{2\pi} KL(\alpha, x_j)\mathrm{d}\alpha = \int_0^{2\pi} \frac{KL_{\text{isocenter}} R}{L(\alpha, x_j)}\mathrm{d}\alpha. \tag{9}$$

In summary, x-ray incidents from the integration of the static source were computed for every measurement point along the horizontal x-axis for all possible beam angles using the air-kerma length product values from a static x-ray source profile. The resulting air-kerma-length-product values from the integration were then compared with the measured air-kerma-length-product values obtained from the rotating x-ray source of the clinical protocols (Sec. 2.4.3).

2.6 *X-Ray Spectrum*

Characterization of the x-ray energy spectra was performed by measuring the TF thickness using a Nomex multimeter (PTW, Freiburg, Germany), positioned at the central beam axis of the isocenter of the scanner, and with an x-ray source static at a 90 deg position. CT localizer radiographs of the SFOV and LFOV with default settings (Sec. 2.4.1) were independently used to measure the TF thickness for tube voltages of 80, 100, 120, and 140 kV. The SpekCalc program[42] was then used to generate x-ray spectra based on the measured TF thickness (Al–equivalent) for both the SFOV and LFOV at each voltage.

Validation of the Nomex multimeter output (TF thickness) for SFOV and LFOV was performed using the measured HVL values at all energy levels between 80 and 140 kV for both SFOV and LFOV (Sec. 2.4.2). Using the SpekCalc program, x-ray spectra were generated for an anode angle of 7 deg, while the aluminum thickness (mm) was increased until the simulated HVL value equaled that of the experimentally measured HVL value.

2.7 *Bowtie Filter Calculation*

The primary focus of this study was to provide an estimation of the BT filter thickness that matched as closely as possible the actual BT filter thickness of the specific CT scanner used. In this section, the algorithm used to calculate the BT filter thickness as a function of fan angle is further explained. The required inputs were (1) the measured air-kerma values at each of the measurement points of the CT localizer radiographs and (2) the x-ray spectra calculated using the measured TF thickness of each kVp. The calculation of the BT filter thickness was done separately using the experimental measurements of SFOV and LFOV.

Air kerma of the static x-ray source was measured for a set of points on the path of the x-ray beam. If the BT filter was placed in the path of the x-ray source, the BT filter thickness would need to be known to produce meaningful measurement values. To achieve this, the initial values of the BT filter thickness in a specified range were set for each of the test points. The range was necessary to allow adjustments in the filter thickness. For each of the points, the attenuation of the x-ray spectrum was calculated for the filter thickness (and angle) through which it passed. This approach takes into account the geometry of the experiment, specifically the distance from the source to the isocenter, the distance between each measurement point, and the distance from the measurement point to the isocenter. It also accounts for both the perpendicular and the off-perpendicular aspect of the beam's transmission through the filter. Usually a beam will travel a greater distance through the same thickness of the filter material if traveling nonperpendicularly to the filter's surface, as opposed to perpendicularly to the surface. After simulating the filter attenuation of the x-ray spectrum, the resulting transmitted radiation through the filter at each of the test points was obtained by assuming an exponential attenuation profile. Consequently, the calculated air kerma was compared with the measured air kerma at each test point. Where the calculated air kerma was greater than the measured kerma value, the filter thickness was increased at that point. Similarly, when the calculated air kerma was less than the measured kerma value, the filter thickness was decreased at that point. After updating the values and ranges of filter thickness at all test points, a chi-squared test was performed. In this case, the calculated air kerma corresponding most closely to the measured air kerma was found when x^2 was minimized

$$x^2 = \frac{(K_{\text{calc}} - K_{\text{meas}})^2}{K_{\text{calc}}}. \tag{10}$$

The following are the sequential steps of calculating the BT thickness.

- Simulating the filter attenuation.
- Calculating the air kerma.
- Adjusting the BT filter thickness.
- Reducing the range of the BT filter thickness and calculating the chi-square statistic.
- Iteratively repeating this step until a minimum value of x^2 is achieved.
- Accepting the BT thickness profile corresponding to the x^2 minimum as the BT filter shape.

This method was implemented using routines coded in the computer language C. The result was a complete set of equivalent BT filter thicknesses based on each of the generated x-ray spectra. It is worth mentioning that the main BT filter material was presumed to be Teflon (PTFE).[26,27,43]

2.8 *Physical Measurement of the CTDI Phantoms*

Measurements were performed on the standard CTDI body (320 mm in diameter), CTDI head (160 mm in diameter), and CTDI child (100 mm in diameter) phantoms. These phantoms are 150 mm in length and made of polymethylmethacrylate (PMMA) material. The phantoms have five holes into which a PMMA rod or the ionization chamber is inserted. All of the scans were performed using the helical mode in which the scan length covers the entire phantom. The child neck clinical protocol for the SFOV was used with scan settings of 90 mA tube current, 5 s scan time, 0.6 pitch, and 38.4 mm beam collimation. The adult thorax clinical protocol for the LFOV was used with scan settings of 110 mA tube current, 0.6 pitch, 2 s scan time, and 38.4 mm beam collimation. Air kerma was measured at all available tube voltages (80, 100, 120, and 140 kV) by inserting the ionization chamber into each of these phantoms at the center hole and also at the four periphery holes (right, left, top, and bottom).

2.9 *Overview of the Monte Carlo Method*

2.9.1 *Monte Carlo simulations*

Verification of the experimental measurements in this study was performed using an existing user code at Helmholtz-Zentrum München, which was applied for dosimetry purposes.[44,45] This user code uses EGSnrc (version V4-2-3-0) for modeling particle transport and scoring energy depositions.[46] The utilized EGSnrc is a developed version of EGS4 in terms of the physics and algorithm used for photon and electron transport, taking into account bound Compton scattering and photoelectrons from K, L, and M valence shells.[47] In addition, the Auger and Coster–Kronig electrons resulting from Compton scattering and the photoelectric effect are also taken into account. The input data for photon cross sections used in the EGS4 were updated by Seuntjens et al.,[48] employing the XCOM program.[49] The material cross sections for photoelectric absorption and Rayleigh scattering in EGSnrc are now consistent with the values in the XCOM/NIST database. The electron collision stopping powers have been revised to agree with those values recommended by ICRU.[50] Moreover, spin effects have been implemented, and the electron multiple scatter algorithm of EGS4 has been extended to PRESTA-II.[51] For the purpose of this study, photons were simulated with a low-energy cutoff of 2 keV. The remaining particle kinetic energy was deposited locally.

2.9.2 *Modeling of the CT source*

The source subroutine of the EGSnrc simulation code was written so that different settings of the CT scanner could be modeled using user-definable input parameters, including geometric factors, x-ray spectra, modes of acquisition, and BT filtration thickness. Geometric factors selected for each simulation included the dimensions of the x-ray source with respect to the simulated object in the x, y, and z axes, SID, focal spot size, and beam collimation along the z axis. This information was obtained from the documentation supplied with the CT scanner (Sec. 2.4.1).

The x-ray source model assumes the photons are emitted from a location within the x-ray tube anode. The x-ray spectra generated by the SpekCalc program based on the measured TF thickness for each tube voltage were used to simulate the x-ray spectra for the CT scanner (Sec. 2.6).

Different modes of acquisition were implemented in the EGSnrc code, including axial, helical (with the ability to input desired pitch), and static beam position (with the ability to select the angle at which the beam is parked). In this study, the static and contiguous axial scans were simulated, corresponding to measurements made using the CT scanner.

The Teflon BT filter thickness was simulated based on a polynomial shape resulting from fitting the rational function to the calculated thickness across all measurement points. The radiation transport process through the filter was simulated by reducing the statistical weight of each incident photon according to its attenuation by the filter. Thus, scatter radiation emitted by the filter was ignored. This has been shown to be justified in a side computation.

2.9.3 *Simulation of the experimental objects*

The plastic ruler used in the experiment was simulated to accurately represent the measurement points on the static x-ray source. The geometric dimensions and position of the ruler were simulated as explained in Sec. 2.4.1. The ruler was discretized into segments, where the total number of voxels were 1560, 120, and 4 in the x, y, and z directions, respectively. The voxel dimensions were $0.5\ \text{mm} \times 0.5\ \text{mm} \times 2\ \text{mm}$ for the x, y, and z-axes, respectively. The voxel material was PMMA. The holes were modeled in a small circular pattern with a diameter of 10 mm, by which the air kerma was calculated.

The standard CTDI phantoms (body, head, and child) were simulated to verify the physical measurements of the rotating x-ray source. A Cartesian coordinate system was defined using the model dimensions so that the isocenter of the modeled phantoms coincided with the isocenter of the scanner, the z-axis was collinear with the axis of the scanner, and the $x-y$ plane was coplanar with the CT slice plane. The computational models had nonisotropic voxels and were described as a set of slices, where each slice consisted of a number of voxels. The number of voxels in the x, y, and z axes was 640, 640, and 6 for the CTDI body, 320, 320, and 6 for the CTDI head, and 200, 200, and 6 for the CTDI child. The voxel dimensions for all computational models were 0.5, 0.5, and 25 mm in the x, y, and z axes, respectively. Within the designated volume, voxels were defined to contain PMMA material and have air present around the simulated voxels. In the central four slices, five 9 mm diameter, cylindrical holes were inserted. In these holes, dose values were recorded to provide air kerma estimates. The CT scanner table was approximated as a 10-mm-thick rectangular carbon slab and modeled with each phantom.

After experimental measurements were recorded for the static and rotating x-ray sources, the source subroutine was used to simulate all measurement configurations for each experiment based on the parameters for the geometric factors, the x-ray spectra, the modes of acquisition, the BT filter profile, and the simulated object. In each simulation, 100 million photon histories were pursued, resulting in a statistical uncertainty of less than 1%. This number of histories was chosen to achieve a compromise between the relative error and reasonable computational times.

3 Results

3.1 *SFOV Integration*

Figures 6(a) and 6(b) show normalized attenuation profiles of the BT filter measurements for a rotating x-ray source, and the measurements from a static x-ray source integrated in a complete 360-deg cycle at 120 kV for child neck and child abdomen protocols, respectively. A strong correlation was observed between the integrated static source and the rotating source for SFOV at all measurement points. The root mean square error (RMSE) was 0.83% for the child neck protocol and 1.11% for the abdomen protocol.

3.2 *LFOV Integration*

The results of the comparison between the attenuation profile of the BT filter measurements from a rotating source and the integrated measurements from a static x-ray source are shown in Figs. 7(a) and 7(b). The measurement and integration data sets were each normalized to the peak value at the isocenter (0 deg). A strong correlation was observed between the integrated static source and the rotating source for LFOV in the adult protocols. In this case, the RMSE was 1.83% for the thorax protocol and 2.09% for the abdomen protocol.

3.3 *X-Ray Spectrum*

The results of the measured HVL described in Sec. 2.4.2 are presented in Tables 1 and 2 for SFOV and LFOV, respectively, for all energy levels between 80 and 140 kV. These tables also include the results of the measured TF thickness values from the Nomex multimeter and the TF thickness values from the SpekCalc program for SFOV and LFOV at each of the available beam energies. A strong correlation was noted between the measured TF thicknesses from the Nomex multimeter device and the estimated TF thicknesses from the SpekCalc program, resulting from matching the HVL measurements for both SFOV and LFOV. The maximum percentage difference was 2.53% at 80 kV for SFOV and 1.68% at 80 kV for LFOV. The percentage difference at each energy level was within the accuracy limit of ±10% for the TF estimation of the Nomex multimeter device (Sec. 2.3).

3.4 *Bowtie Filter Calculation*

3.4.1 *Bowtie filter thickness for SFOV*

Figure 8 shows derived BT filter thicknesses for SFOVs. The filters are made of aluminum and Teflon, and the measurements are based on SFOVs for beam energies of 80 to 140 kV. The maximum calculated BT filter thickness observed at the periphery was 8.57 cm, and the maximum measured TF thickness at the center was 1.2 cm for all energy levels between 80 and 140 kV. BT filters of equal thickness from the two materials showed strong correlations at each energy level. The maximum variation across all calculated BT thicknesses was 8.66% for all tube voltages, with a slight deviation in the BT filter thickness at 140 kV.

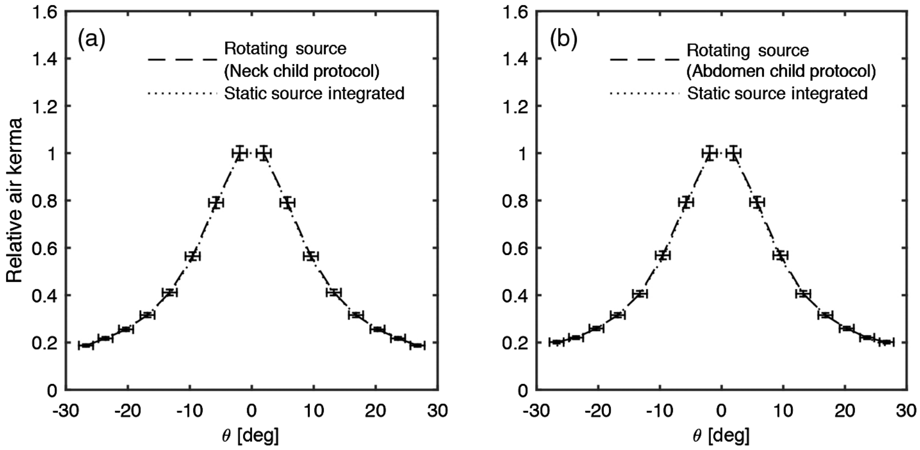

Fig. 6 Comparison of normalized profiles of BT filter from the integrated air kerma and the measured air kerma for the SFOV at 120 kV. (a) Static source integrated and child neck protocol. (b) Static source integrated and child abdomen protocol.

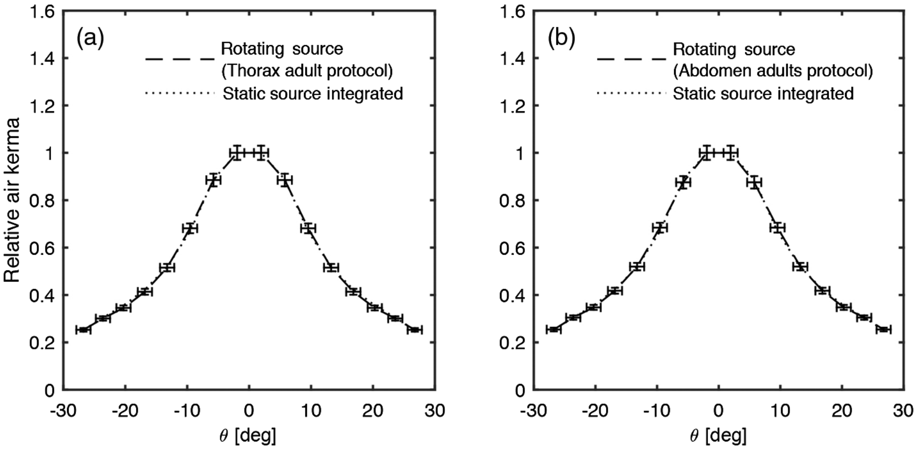

Fig. 7 Comparison of normalized profiles of BT filter from the integrated air kerma and the measured air kerma for the LFOV at 120 kV. (a) Static source integrated and adult thorax protocol. (b) Static source integrated and adult abdomen protocol.

Table 1 Measured TF thickness in mm Al from the Nomex multimeter device and the resulting TF thickness in mm Al from the SpekCalc program, resulting from matching the measured HVL in mm Al for all tube voltages ranging from 80 kV to 140 kV for SFOV.

Energy level	Measured HVL (mm)	Measured TF from Nomex multimeter (mm)	TF from the SpekCalc program (mm)	Percentage difference (%)
80	6.07 ± 0.1	12 ± 0.5	11.70	2.53
100	7.40 ± 0.1	12 ± 0.5	11.75	2.10
120	8.50 ± 0.1	12 ± 0.5	11.95	0.42
140	9.40 ± 0.1	12 ± 0.5	11.95	0.42

Table 2 Measured TF thickness in mm Al from the Nomex multimeter device and the resulting TF thickness in mm Al from the SpekCalc program, resulting from matching the measured HVL in mm Al for all tube voltages ranging from 80 kV to 140 kV for LFOV.

Energy level	Measured HVL (mm)	Measured TF from Nomex multimeter (mm)	TF from the SpekCalc program (mm)	Percentage difference (%)
80	6.10 ± 0.1	12 ± 0.5	11.80	1.68
100	7.45 ± 0.1	12 ± 0.5	11.95	0.42
120	8.52 ± 0.1	12 ± 0.5	12.05	0.42
140	9.45 ± 0.1	12 ± 0.5	12.18	1.49

3.4.2 *Bowtie filter thickness for LFOV*

The resulting estimates of BT filter thickness for all tube voltages from 80 to 140 kV are shown in Fig. (9) for LFOV. The BT filter thickness at the periphery was 6.05 cm, and the TF thickness at the center was 1.2 cm. A strong correlation was found among the calculated BT thicknesses across all fan angles, with a maximum variation of 4.90% for all tube voltages ranging from 80 to 140 kV.

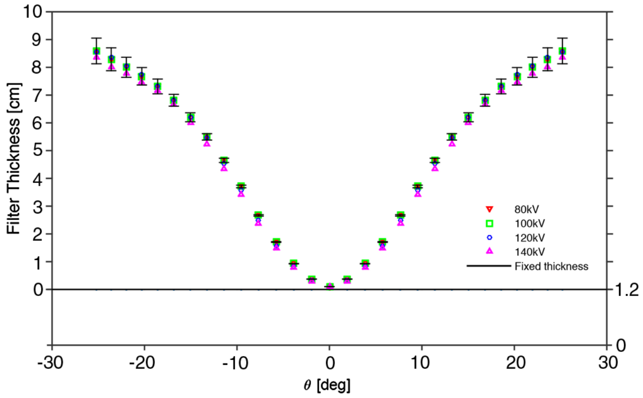

Fig. 8 Calculated BT filter thickness for SFOV at energy levels of 80, 100, 120, and 140 kV. The measured BT filter thickness is shown for aluminum filters (horizontal black line) and Teflon filters (colored lines).

3.5 *Monte Carlo Simulation*

MC simulations were executed a total of eight times to simulate static x-ray sources. Four simulations were run for energy levels of 80, 100, 120, and 140 kV, for both SFOV and LFOV. For each of the conducted simulations, 100 million photon histories were pursued, resulting in coefficients of variance (standard deviation to variance ratio) in the calculated air kerma for each of the ruler holes of less than 0.40%.

3.5.1 *Simulation of the static source geometry for SFOV*

Figure 10 shows a normalized attenuation profile of the BT filter obtained from the static x-ray source simulated by MC. This can be directly compared with the BT filter profile measured for a static x-ray source using the CT localizer radiograph for SFOV between the energy levels 80 and 140 kV. A strong correlation was observed between the BT profiles of the simulated and the measured air kerma for all measurement points. The RMSE

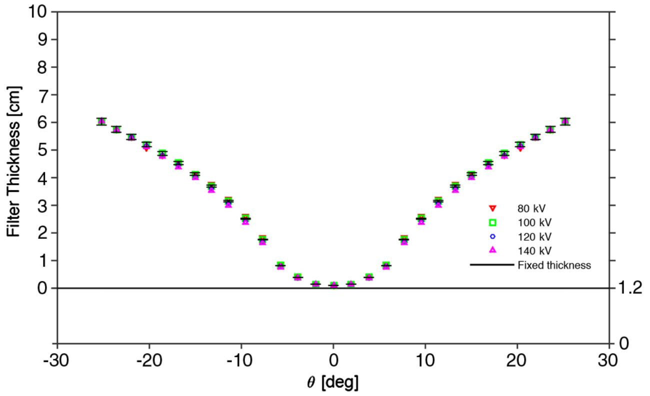

Fig. 9 Calculated BT filter thickness for LFOV at energy levels of 80, 100, 120, and 140 kV. The measured BT filter thickness is shown for aluminum filters (horizontal black line) and Teflon filters (colored lines).

values were 1.64%, 0.43%, 0.31%, and 1.16% for tube voltages of 80, 100, 120, and 140 kV, respectively.

3.5.2 *Simulation of the static source geometry for LFOV*

The static x-ray source of the CT localizer radiograph revealed similar agreements for the simulated and measured BT profile results for LFOV, as shown in Fig. 11. The RMSE values were 1.05%, 1.40%, 1.80%, and 2.50% for tube voltages of 80, 100, 120, and 140 kV, respectively. Significantly, the difference between the simulated and measured results for both the SFOV and LFOV at all measurement points and tube voltages remained below the 5% homogeneity threshold of the ionization chamber response.

3.5.3 *Simulation results for the rotating source geometry for SFOV*

The MC calculations were carried out for all energy levels and phantoms. Four simulations were run for each computational phantom, each with 100 million photon histories. This resulted in coefficients of variance in the calculated air kerma values for individual holes between 0.40% and 1.0%.

The measurement and simulation data sets were each normalized to the peak value at the top hole. Figure 12 shows the relative measured and simulated air kerma of the rotating x-ray source for SFOVs on the standard (a–d) CTDI body, (e–h) CTDI head, and (i–l) CTDI child phantoms, at tube voltages between 80 and 140 kV. The results for the CTDI body phantom revealed a strong correlation between the measured and simulated air kerma for all measurement holes. The maximum deviations were 1.4%, 4.9%, 7.2%, and 3.2% for tube voltages of 80, 100, 120, and 140 kV, respectively.

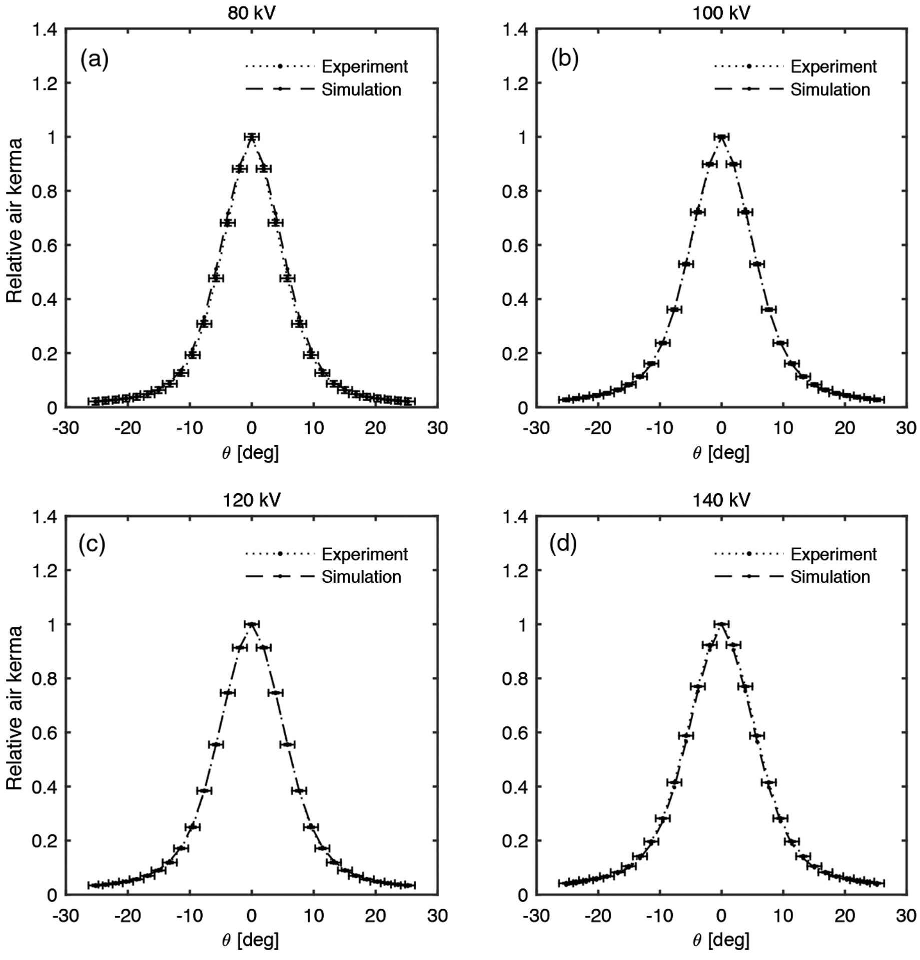

Fig. 10 Comparison of normalized profiles between simulated and measured air kerma of the static x-ray source of the SFOV for (a) 80, (b) 100, (c) 120, and (d) 140 kV.

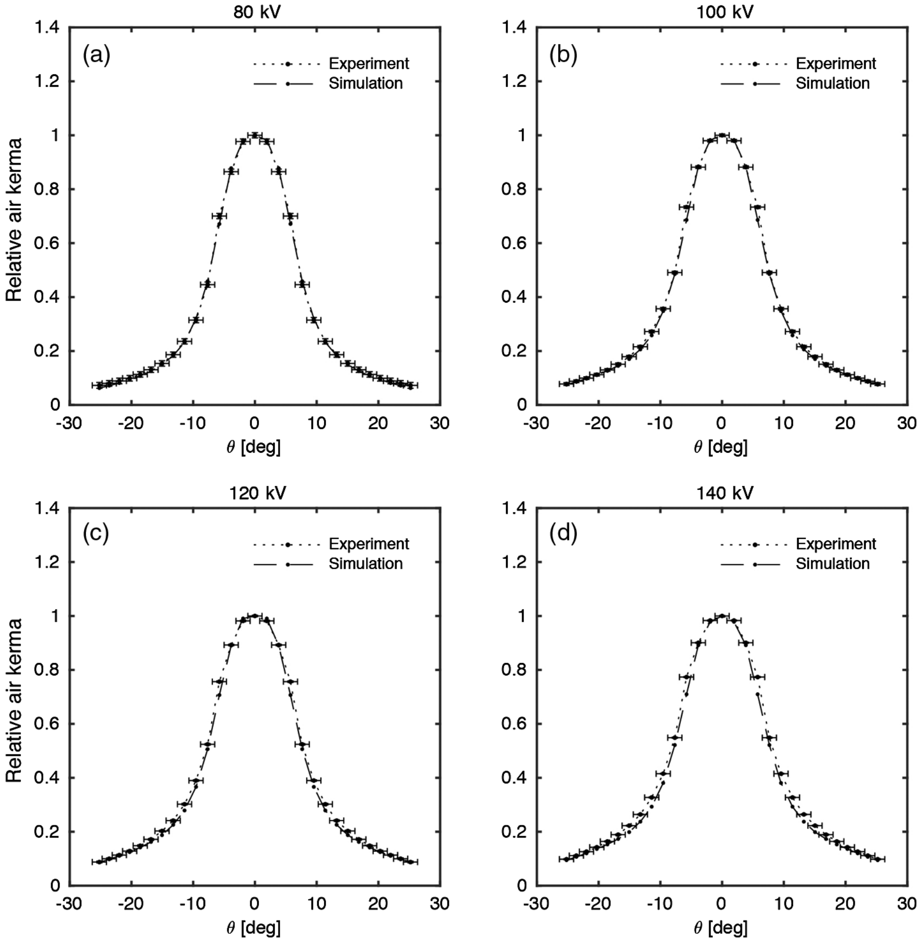

Fig. 11 Comparison of normalized profiles between simulated and measured air kerma of the static x-ray source of the LFOV for (a) 80, (b) 100, (c) 120, and (d) 140 kV.

Results for the CTDI head phantom showed similar agreements between the measured and simulated air kerma for all the measurement holes, with maximum deviations of 5.01%, 1.42%, 2.85%, and 2.90% for tube voltages of 80, 100, 120, and 140 kV, respectively.

Results for the CTDI child phantom also showed similar agreements between the simulated and measured air kerma, with maximum deviations of 1.45%, 3.91%, 3.15%, and 3.70% for tube voltages of 80, 100, 120, and 140 kV, respectively.

3.5.4 *Simulation results for the rotating source geometry for LFOV*

The relative measured and simulated air kerma of the rotating x-ray source for LFOVs were verified using the standard CTDI body, CTDI head, and CTDI child phantoms at tube voltages between 80 and 140 kV. The patterns of the simulated and measured data were similar to those shown in Fig. 12. The measured air kerma of the CTDI body phantom was not significantly different than the simulated air kerma from the MC simulation of the same phantom for all measurement holes. The maximum deviations were 6.01%, 3.28%, 2.29% and 1.7% for tube voltages of 80, 100, 120, and 140 kV, respectively.

Similar correlations were observed in the results for the CTDI head phantoms for all measurement holes. The maximum deviations were 4.77%, 2.47%, 3.36%, and 3.99% for tube voltages of 80, 100, 120, and 140 kV, respectively.

Results for the CTDI child phantoms show strong correlations between the measured and simulated air kermas. The maximum deviations were 2.56%, 5.91%, 5.74%, and 6.31% for tube voltages of 80, 100, 120, and 140 kV, respectively.

4 Discussion

The integration method introduced in this study involves integrating the measured profile of the BT filter across the fan angle utilizing a static x-ray source. This method enables a direct comparison of the BT filter profiles using only physical measurements of static and rotating sources. The results of this study indicate a strong correlation between the integrated BT profile from the static source of the scanner and the measured BT profile from the rotating source used in the clinical protocol. The integration method was able to accurately simulate the BT filter of the static x-ray source and the rotating source used in the clinical protocol. This ability makes it unnecessary to use time-resolving measurements and to instead simply use physical measurements of the static source to determine the BT filter thickness for different modes of the scanning process.

The comprehensiveness of this method was further tested by comparing the integrated static x-ray source air-kerma profiles (based on the physical measurements taken from a particular CT localizer radiograph) to the measured air-kerma profiles from a separate clinical protocol. This comparison was possible due to the similarities between the FOVs of the localizers and the

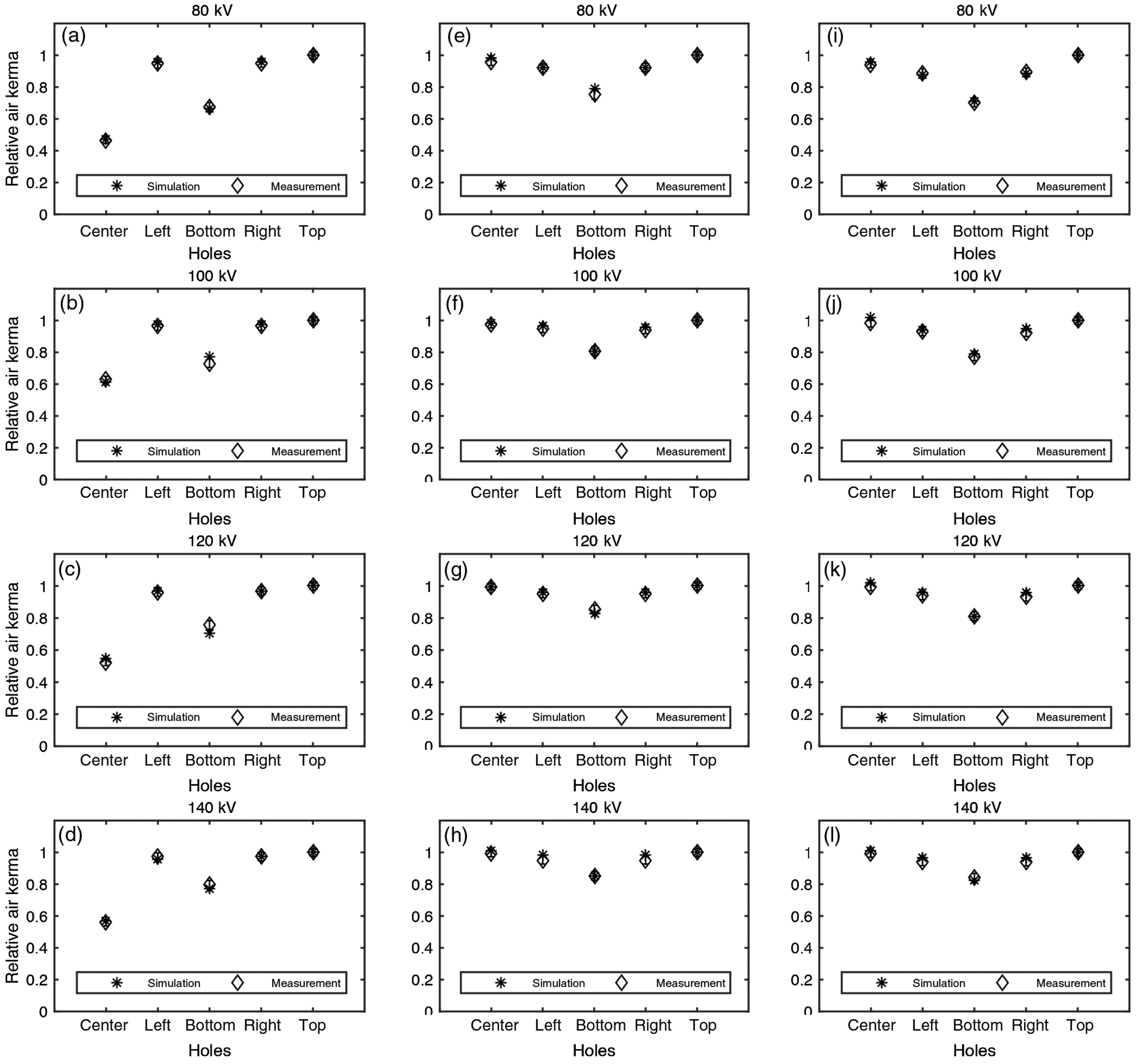

Fig. 12 Comparison of relative measured and simulated air kerma of the (a–d) CTDI body, (e–h) CTDI head, and (i–l) CTDI child phantoms of the rotating x-ray source for SFOV at tube voltages of 80, 100, 120, and 140 kV.

clinical protocols. A similar level of agreement was noted between the integrated static x-ray source air-kerma profiles (using the CT localizer radiographs of the child neck SFOV and adult abdomen LFOV) as that between the measured air-kerma profiles of the child abdomen and adult thorax protocols in the case of SFOV and LFOV, respectively. These results provide substantial support for the conclusion that the BT filters utilized by CT localizer radiographs sufficiently represent the thickness and composition of the filters used in clinical protocols. This consistency could be due to the similarities between the default settings used in clinical protocols and the CT localizer radiographs. Because the latter is a part of clinical protocols, it may substantially contribute to the overall radiation dose delivered by full CT scan examinations, particularly in the case of dedicated low-dose scans of young patients or for screening purposes.[52] Consequently, accurate determination of the BT filter thicknesses could help estimate dose values resulting from CT localizer radiographs.[53–55] In addition, the free accessibility of the static x-ray source used by the CT localizer radiograph is an added benefit compared with the service mode, for which a special personnel agreement is required.

Characterization of the x-ray tube output, as represented by the x-ray spectrum, is essential for an accurate determination of the BT filter thickness at tube voltages of 80, 100, 120, and 140 kV. However, the x-ray spectrum for a given voltage is proprietary, which necessitates an alternative method for estimation. Usually, such methods are based on the principle of HVL measurements, where the HVL is defined as the thickness of aluminum required to reduce the air kerma by one-half. The HVL is energy dependent, and it increases as the x-ray tube potential increases (for example, a tube voltage of 80 kV has a lower HVL than a tube voltage of 140 kV). This results in a more hardened x-ray spectrum for high voltages than for low ones. Therefore, the x-ray spectra generated based on the HVL and used to estimate BT filter thicknesses result in BT filter thickness values that correspond to tube voltage. Hence, the resulting attenuation due to BT filter thickness decreases with tube voltage. This could partly explain the discrepancy in the calculated BT filter thickness values for tube voltages of 80, 100, 120, and 140 kV and the results of MC simulations based on the calculated BT filter thickness in previous studies.[30,32,33]

In this study, the concept of TF was used to estimate the TF thickness at the isocenter, independent of tube voltage. The measured TF thickness of the static CT localizer radiograph was 12 ± 0.5 mm (Al) for SFOV and LFOV at all tube voltages. These measurements were verified by comparing the measured HVL with the HVL of the x-ray spectra generated by the SpekCalc program. The TF thicknesses measured by the Nomex multimeter device were found to be in good agreement with the resulting TF thicknesses generated by the SpekCalc program that resulted from the measured HVL values at each energy level of 80 to 140 kV for SFOV and LFOV. For SFOV, the maximum percentage difference was 2.53% at 80 kV and the minimum percentage difference was 0.42% at both 120 and 140 kV. For LFOV, the maximum percentage difference was 1.68% at 80 kV and 0.42% at both 100 and 120 kV. A similar result was found in an earlier study where researchers observed a total beam filtration of up to 12 mm for A1 equivalent filtration in the CT scanners.[56] The x-ray spectra generated using the TF thickness were used to calculate the BT filter thickness for each tube voltage. This could explain why the calculated BT filter thickness was the same for all energy levels. This consistency, in turn, provides support for the hypothesis that BT filter thickness is dependent on energy level and, more specifically, the FOV. The slight deviation observed in the calculated BT filter thickness could be the result of measurement error of the localizer radiographs, in addition to the 10% uncertainty stemming from the algorithm utilized to calculate the BT filter thickness.

Accurate estimates of the x-ray spectra and the estimated BT filter thickness of the x-ray tube are essential to effectively comparing the calculated air kerma from the MC simulation with the measured air kerma from the experiments. In addition, a strong geometrical correlation is also necessary between the dosimetry phantoms and the computational model. In the current study, the simulated air kerma and the measured air kerma of the static x-ray source showed strong agreement at each tube voltage. The RMSE values across all the measurement angles for both SFOV and LFOV fall within the functionality of the ionization chamber, with a 5% uncertainty for all tube voltages between 80 and 140 kV. This indicates that the calculated BT filter thicknesses correspond to those of the given CT scanner. Moreover, the x-ray spectrum SpekCalc software, which is based on the measured TF at the isocenter, gives a good approximation of the x-ray tube's output.

The calculated BT filter thickness of the rotating x-ray source showed significant agreement with both the simulated and measured SFOVs across all measurement holes. The maximum deviation of 7.2% was observed at 120 kV for the CTDI body phantom. A similar correspondence was found between the simulated and measured air kerma for LFOV. Here, the maximum deviations observed across all measurement holes of the CTDI body phantom were less than 6.01% at 80 kV and less than 5.91% at 140 kV for the CTDI child phantom. This level of uncertainty could be attributed to measurement error or error due to external factors such as variations in temperature, pressure, and x-ray source output. An additional reason for the deviation between the simulated and measured air kerma could be the combined effects of using a geometry voxel representation-based MC and the MC source code.

5 Conclusion

The integration method described in this study successfully resulted in an accurate estimation of the BT profile for the rotating x-ray source, based on the measured BT profile of the static x-ray source. This suggests that the integration method can result in a very strong correlation between the integrated and measured profiles. This indicates the possibility of deducing the BT filter thickness of the clinical protocol based on the physical measurements of the CT localizer radiograph alone. The physical measurements, along with the calculations, were adequate for estimating an accurate BT filter thickness for each energy spectrum that was attenuated by the TF thickness. The strong correlation between the simulated and actual physical measurements of air kerma for both the static and rotating x-ray sources supports this conclusion. These results will help to more accurately estimate the dose delivered to specific organs of the body and thereby contribute to cancer risk management in diagnostic radiology.

Disclosures

No conflicts of interest.

Acknowledgments

The authors gratefully acknowledge a grant by "Deutscher Akademischer Austauschdienst" (DAAD, German Academic Exchange Service, Germany, grant program number: 57048249).

References

1. C. H. McCollough et al., "Achieving routine submillisievert CT scanning: report from the summit on management of radiation dose in CT," *Radiology* **264**(2), 567–580 (2012).
2. D. J. Brenner and E. J. Hall, "Computed tomography: an increasing source of radiation exposure," *N. Engl. J. Med.* **357**(22), 2277–2284 (2007).
3. F. A. Mettler, Jr. et al., "Radiologic and nuclear medicine studies in the United States and worldwide: frequency, radiation dose, and comparison with other radiation sources—1950–2007," *Radiology* **253**(2), 520–531 (2009).
4. National Council on Radiation Protection and Measurements, "Ionizing radiation exposure of the population of the United States," NCRP Report No. 160, National Council on Radiation Protection and Measurements, Bethesda, Maryland (2009).
5. BEIR, "Health risks from exposure to low levels of ionizing radiation," BEIR VII Report, BEIR VII Phase 2, National Academies Press, Washington, DC (2006).
6. P. Akhlaghi et al., "A Monte Carlo study on quantifying the amount of dose reduction by shielding the superficial organs of an Iranian 11-year-old boy," *J. Med. Phys.* **41**(4), 246–253 (2016).
7. G. Jarry et al., "A Monte Carlo-based method to estimate radiation dose from spiral CT: from phantom testing to patient-specific models," *Phys. Med. Biol.* **48**(16), 2645–2663 (2003).
8. M. Salvadó et al., "Monte Carlo calculation of radiation dose in CT examinations using phantom and patient tomographic models," *Radiat. Prot. Dosim.* **114**(1–3), 364–368 (2005).

9. J. J. DeMarco et al., "A Monte Carlo based method to estimate radiation dose from multidetector CT (MDCT): cylindrical and anthropomorphic phantoms," *Phys. Med. Biol.* **50**(17), 3989–4004 (2005).
10. M. Caon, "The reduction in Monte Carlo calculated organ doses from CT with tube current modulation using WILLIAM, a voxel model of seven year-old anatomy," *Australas. Phys. Eng. Sci. Med.* **37**(4), 743–752 (2014).
11. A. J. Einstein et al., "Radiation dose and cancer risk estimates in 16-slice computed tomography coronary angiography," *J. Nucl. Cardiol.* **15**(2), 232–240 (2008).
12. A. C. Turner et al., "The feasibility of a scanner-independent technique to estimate organ dose from MDCT scans: using CTDIvol to account for differences between scanners," *Med. Phys.* **37**(4), 1816–1825 (2010).
13. X. Li et al., "Patient-specific radiation dose and cancer risk for pediatric chest CT," *Radiology* **259**(3), 862–874 (2011).
14. X. Li et al., "Patient-specific radiation dose and cancer risk estimation in CT: part II. Application to patients," *Med. Phys.* **38**(1), 408–419 (2011).
15. T. Oono et al., "Monte Carlo calculation of patient organ doses from computed tomography," *Radiol. Phys. Technol.* **7**(1), 176–182 (2014).
16. J. J. DeMarco et al., "Estimating radiation doses from multidetector CT using Monte Carlo simulations: effects of different size voxelized patient models on magnitudes of organ and effective dose," *Phys. Med. Biol.* **52**(9), 2583–2597 (2007).
17. X. Tian et al., "Pediatric chest and abdominopelvic CT: organ dose estimation based on 42 patient models," *Radiology* **270**(2), 535–547 (2014).
18. E. Angel et al., "Dose to radiosensitive organs during routine chest CT: effects of tube current modulation," *AJR Am. J. Roentgenol.* **193**(5), 1340–1345 (2009).
19. V. S. Sechopoulos et al., "Monte Carlo and phantom study of the radiation dose to the body from dedicated CT of the breast," *Radiology* **247**(1), 98–105 (2008).
20. A. E. Papadakis, K. Perisinakis, and J. Damilakis, "Development of a method to estimate organ doses for pediatric CT examinations," *Med. Phys.* **43**(5), 2108–2117 (2016).
21. Y. Gao et al., "A comparison of pediatric and adult CT organ dose estimation methods," *BMC Med. Imaging* **17**(1), 28 (2017).
22. H. Zaidi and M. R. Ay, "Current status and new horizons in Monte Carlo simulation of x-ray CT scanners," *Med. Biol. Eng. Comput.* **45**(9), 809–817 (2007).
23. M. R. Ay and H. Zaidi, "Development and validation of MCNP4C-based Monte Carlo simulator for fan- and cone-beam x-ray CT," *Phys. Med. Biol.* **50**(20), 4863–4885 (2005).
24. D. M. Tucker, G. T. Barnes, and D. P. Chakraborty, "Semiempirical model for generating tungsten target x-ray spectra," *Med. Phys.* **18**(2), 211–218 (1991).
25. A. C. Turner et al., "A method to generate equivalent energy spectra and filtration models based on measurement for multidetector CT Monte Carlo dosimetry simulations," *Med. Phys.* **36**(6), 2154–2164 (2009).
26. J. M. Boone, "Method for evaluating bow tie filter angle-dependent attenuation in CT: theory and simulation results," *Med. Phys.* **37**(1), 40–48 (2010).
27. S. E. McKenney et al., "Experimental validation of a method characterizing bow tie filters in CT scanners using a real-time dose probe," *Med. Phys.* **38**(3), 1406–1415 (2011).
28. B. R. Whiting et al., "Measurement of bow tie profiles in CT scanners using a real-time dosimeter," *Med. Phys.* **41**(10), 101915 (2014).
29. M. Randazzo and M. Tambasco, "A rapid noninvasive characterization of CT x-ray sources," *Med. Phys.* **42**(7), 3960–3968 (2015).
30. B. Alikhani and L. Büermann, "Non-invasive experimental determination of a CT source model," *Phys. Med.* **32**(1), 59–66 (2016).
31. M. Sommerville, Y. Poirier, and M. Tambasco, "A measurement-based x-ray source model characterization for CT dosimetry computations," *J. Appl. Clin. Med. Phys.* **16**(6), 386–400 (2015).
32. X. Lopez-Rendon et al., "Implementing the complete beam hardening effect of the bowtie filter versus scaling beam intensities: effects on dosimetric applications in computed tomography," *J. Med. Imaging* **1**(3), 033507 (2014).
33. X. Li et al., "A new technique to characterize CT scanner bow-tie filter attenuation and applications in human cadaver dosimetry simulations," *Med. Phys.* **42**(11), 6274–6282 (2015).
34. Y. Lin et al., "An angle-dependent estimation of CT x-ray spectrum from rotational transmission measurements," *Med. Phys.* **41**(6), 062104 (2014).
35. K. Yang et al., "Direct and fast measurement of CT beam filter profiles with simultaneous geometrical calibration," *Med. Phys.* **44**(1), 57–70 (2017).
36. Center for Evidence Based Purchasing CEP, "Comparative specifications 32 to 40 slice CT scanners," Report No. CEP08026, NHSPASA, London (2009).
37. PTW Freiburg, GmbH, "CT chambers type 30009," PTW, http://www.ptw.de/fileadmin/data/download/catalogviewer/DETECTORS_Cat_en_16522900_10/blaetterkatalog/index.html?startpage=38#page_38 (22 February 2017).
38. IEC 61674, "Medical electrical equipment—dosimeters with ionization chambers and/or semiconductor detectors as used in x-ray diagnostic imaging," TC 62/SC 62C, ICS. 11.040.50 - Radiographic Equipment, International Electrotechnical Commission, Switzerland (2012).
39. PTW Freiburg, GmbH, "NOMEX PTB type approved," PTW, http://www.ptw.de/1861.html?&no_cache=1&tx_ttnews%5Btt_news%5D=132 (14 February 2012).
40. PTW Freiburg, GmbH, "True precision. PTW. NOMEX® multimeter," PTW, http://www.ptw.de/2361.html?&cId=7082%22%27%60 (3 February 2017).
41. PTW Freiburg, GmbH, "NOMEX multimeter," PTW, http://www.ptw.de/2362.html?&cId=7082%22%27%60 (3 February 2017).
42. G. Poludniowski et al., "SpekCalc: a program to calculate photon spectra from tungsten anode x-ray tubes," *Phys. Med. Biol.* **54**(19), N433–N438 (2009).
43. R Schmidt, J. Wulff, and K. Zink, "GMctdospp: description and validation of a CT dose calculation system," *Med. Phys.* **42**(7), 4260–4270 (2015).
44. H. Schlattl, M. Zankl, and N. Petoussi-Henss, "Organ dose conversion coefficients for voxel models of the reference male and female from idealized photon exposures," *Phys. Med. Biol.* **52**(8), 2123–2145 (2007).
45. H. Schlattl et al., "Dose conversion coefficients for paediatric CT examinations with automatic tube current modulation," *Phys. Med. Biol.* **57**(20), 6309–6326 (2012).
46. I. Kawrakow et al., "The EGSnrc code system: Monte Carlo simulation of electron and photon transport," NRC Report No. PIRS-701, National Research Council of Canada, Ottawa (2013).
47. W. R. Nelson et al., "The EGS4 code system (Stanford, CA: Stanford Linear Accelerator Center)," SLAC Report No 265, Stanford University, Stanford, California (1985).
48. J. P. Seuntjens et al., "Calculated and measured air-kerma response of ionization chambers in low and medium energy photon beams," in *Recent Developments in Accurate Radiation Dosimetry, Proc. Int. Workshop*, pp. 69–84, Medical Physics Publishing, Madison (2001).
49. M. J. Berger and J. H. Hubbell, "XCOM: photon cross sections on a personal computer," NBSIR 87-3597, National Bureau of Standards (former name of NIST), Gaithersburg, Maryland (1987).
50. ICRU, "Stopping powers for electrons and positrons," ICRU Report No 37, International Commission on Radiation Units and Measurements, Bethesda, Maryland (1984).
51. I. Kawrakow and A. F. Bielajew, "On the condensed history technique for electron transport," *Nucl. Instrum. Methods Phys. Res.* **142**(3), 253–280 (1998).
52. B. Schmidt et al., "Assessment of patient dose from CT localizer radiographs," *Med. Phys.* **40**(8), 084301 (2013).
53. D. R. Coles et al., "Comparison of radiation doses from multislice computed tomography coronary angiography and conventional diagnostic angiography," *J. Am. Coll. Cardiol.* **47**(9), 1840–1845 (2006).
54. J. C. O'Daniel, D. M. Stevens, and D. D. Cody, "Reducing radiation exposure from survey CT scans," *AJR Am. J. Roentgenol.* **185**(2), 509–515 (2005).
55. K. Perisinakis et al., "Patient dose reduction in CT examinations by optimizing scanogram acquisition," *Radiat. Prot. Dosim.* **93**(2), 173–178 (2001).

56. H. D. Nagel, *CT Parameters that Influence the Radiation Dose: Radiation Dose from Adults and Pediatric Multidetector Computed Tomography*, pp. 51–79, Springer-Verlag, Berlin (2007).

Ahmad Ibrahim Hassan is currently a PhD student at the Otto von Guericke Universität Magdeburg, Germany. He received his BSc degree in radiation science from the University of Science and Technology in Jordan and his master's degree in medical science from Örebro University, Sweden, in 2008 and 2013, respectively. His PhD subject focuses on the dosimetry calculation of organ dose in computed tomography.

Biographies for the other authors are not available.